Chapter 3
Thermal Conductivity Measurements via the Bolometric Effect

Abstract In this chapter I will introduce the measurement of thermal conductivity using the bolometric effect. The bolometric effect is defined as the resistivity change of a material due to heating. Indeed, the bolometric effect forms the basis of many modern technological sensors and devices. For instance, most commonly used integrated circuit thermometers are based on the well calibrated resistivity change of a Pt strip. Another example is the thermal imaging sensors. A cooled array of high temperature coefficient of resistance material can sensitively detect the infrared spectrum due to the change in the electrical resistance of the active material.

Keywords Bolometric thermal conductivity measurement method · Thermal conductivity in metallic 2D materials · Scanning photocurrent microscopy · Thermal conductivity measurements in 1D

3.1 Introduction

Almost all pure materials whether metallic or semiconducting show a well-defined temperature dependent resistivity in a wide range of temperature. Even if there is no temperature dependence that can be written as a well-defined continuous function, it is possible to describe the temperature dependence for certain temperature intervals. This temperature dependence can be used to determine the temperature distribution over a material even if the heat source is local and there is a temperature gradient over the material. The measurement process can be performed as the following. The electrical resistance of the sample is determined when it is in thermal equilibrium with the environment in the absence of the local heat source. Then, the local heat is applied to the sample and once the steady state is reached the electrical measurement is performed. The difference in the resistivities of the measurements before and after the heating is due to the temperature dependent resistivity change in the material. The thermal distribution can be modelled precisely with a known thermal conductivity. However, the purpose of the method is to measure the thermal conductivity. So, by using the thermal conductivity as a fitting parameter, using the thermal distribution, the resistance of the measured specimen can be calculated to match the experimental

© The Author(s), under exclusive license to Springer Nature Singapore Pte Ltd. 2020

T. S. Kasirga, *Thermal Conductivity Measurements in Atomically Thin Materials and Devices*, Nanoscience and Nanotechnology,
https://doi.org/10.1007/978-981-15-5348-6_3

value. This strategy is not advantageous for measuring bulk materials as there are much more convenient and direct ways of measuring the thermal conductivity. However, in the case of a nanowire or a nanosheet, when the number of available methods are limited, the technique has been proven to be useful.

3.2 Theoretical Background

A focused laser beam is a very convenient way to deliver heat onto many 2D materials as in the case of Raman thermometry. The major concern here is the existence of several photoconductance mechanisms that limits the usability of the technique in semiconducting materials. However, no single technique in the realm of thermal conductivity measurements rule them all as discussed before. So far, by using the laser beam as a local heat source, we measured the thermal conductivity of metallic thin sheets. However, via a detailed analysis, the photoconductance mechanisms can be differentiated experimentally and the bolometric effect can still be used to extract the thermal conductivity.

When a 2D material is laid over a smooth substrate, a considerable portion of the heat will be transferred to substrate through the interface. Such a measurement is very challenging for a 2D material. Thus, ideally if the 2D sheet can be suspended across a trench or over a circular hole, the requirement to measure the thermal boundary conductance will be eliminated. This is discussed in the previous chapters and we showed that the Raman thermometry based method uses the same experimental methodology.

3.2.1 Bolometric Effect

When the electromagnetic radiation impinging on a material causes a change in the electrical resistivity of a material due to the raising temperature, the calibrated change of the electrical resistance of the device can be used as a thermometer. The effect has many applications ranging from astronomy to particle physics and micro-bolometer arrays are used commonly for thermal imaging.

The electrical resistance of most metals and semiconductors depend on the temperature around the room temperature. For the metals, the electrical resistance increases linearly with the increasing temperature. At cryogenic temperatures, typically below 20 K, residual resistivity appears and a plateau in the resistance-temperature curve is observed. For many metals, if the temperature is further decreased, the superconducting state appears where the electrical resistivity vanishes. At very high temperatures deviations from the linearity is observed due to the combined effects of increased scattering, vacancy formation and strain. The general expression for the electrical resistivity ρ can be written as:

$$\rho(T) = \rho_0[1 + \alpha(T - T_0)] \quad (3.1)$$

where T_0 is a fixed reference temperature, α is the temperature coefficient of resistance, ρ_0 is the resistivity at T_0. For the semiconductors, a similar expression can be written. In the case of semiconductors, the number of electrical carriers increase exponentially due to the change in the number of electrons that are be transferred to the conduction band. It is rather straightforward to derive the following relation for an intrinsic semiconductor:

$$\rho(T) = \rho_0 e^{E_A/k_B T} \quad (3.2)$$

Here, E_A is the activation energy and k_B is the Boltzmann constant. Activation energy is half of the band gap for some semiconductors however, it is better to be determined experimentally from the resistance versus temperature (RT) measurements. Details of RT measurements is given in the experimental section.

3.2.2 *Analytical Solution of the Heat Equation for Isotropic 2D Materials*

For the device geometry given in Fig. 3.1. It is straightforward to solve the heat equation over the suspended part of the material as well as the supported part with a Gaussian laser spot delivering the heat to the system. For the sake of simplicity we excluded the Newtonian cooling. Heat equation for the suspended part of the crystal

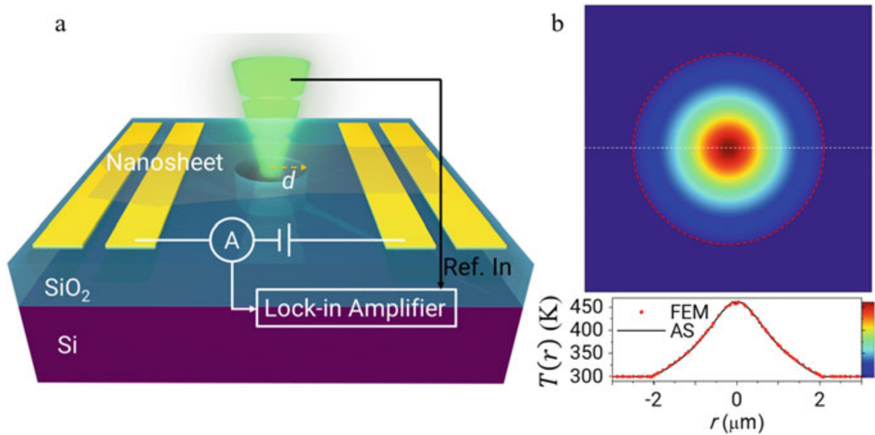

Fig. 3.1 **a** Schematic of the device and the measurement scheme is given. The crystal is suspended over a hole of radius d. **b** Temperature distribution over and in the vicinity of the hole for a typical 2D material under typical laser illumination power. Lower panel shows the line trace taken along the center of the suspended section showing the analytical solution and the FEM solution

in radial coordinates to find the temperature distribution over the hole, $T_1(r)$, can be written as:

$$\kappa \frac{1}{r}\frac{d}{dr}\left[r\frac{d}{dr}T_1(r)\right] + q(r) = 0 \qquad r < R \tag{3.3}$$

where

$$q(r) = \frac{P\alpha}{\pi t r_0^2} e^{-r^2/r_0^2} \tag{3.4}$$

is the heat delivered by the volumetric Gaussian laser spot at the center of the hole. P is the laser power, r_0 is the full width at half maximum of the Gaussian spot, α is the absorbance of the crystal, t is the thickness of the crystal. Outside of the suspended part, where $r > R$, the heat equation is written as the following:

$$\kappa' \frac{1}{r}\frac{d}{dr}\left[r\frac{d}{dr}T_2(r)\right] - G/t[T_2(r) - T_0] = 0 \qquad r > R \tag{3.5}$$

Here, a different value to the thermal conductivity κ' is assigned to the supported part of the material due to the substrate effects on the 2D materials as discussed in Chap. 2. $T_2(r)$ is the temperature distribution over the supported part and T_0 is the ambient temperature. G is the thermal boundary conductance between the crystal and the substrate. Solving Eqs. 3.3 and 3.5 together with the appropriate boundary conditions yields the temperature distribution everywhere on the sample. The general solutions to the above equations give:

$$T_1(r) = c_1 + c_2 ln(r) + \frac{\alpha P}{4\pi t \kappa} Ei(-\frac{r^2}{r_0^2}) \qquad r < R \tag{3.6}$$

$$T_2(\gamma) = c_3 I_0(\gamma) + c_4 K_0(\gamma) + T_0 \qquad r > R \tag{3.7}$$

where $\gamma = r\left[\frac{G}{\kappa' t}\right]^{1/2}$, introduced for the ease of calculations. I_0 and K_0 are the zeroth order modified Bessel's functions of the first and the second kind, respectively. Ei is the exponential integral. As for the boundary conditions we use the following to find the constants c_1, c_2, c_3 and c_4:

$$(i) \qquad T_1(R) = T_2(R) \tag{3.8}$$

$$(ii) \qquad T_2(\gamma \to \infty) = T_0 \tag{3.9}$$

$$(iii) \qquad \left.\frac{dT_1(r)}{dr}\right|_{r\to 0} = 0 \tag{3.10}$$

$$(iv) \qquad \kappa \left.\frac{dT_1(r)}{dr}\right|_{r\to R} = \kappa' \left.\frac{dT_2(\gamma)}{dr}\right|_{r\to R} \tag{3.11}$$

Under these boundary conditions we find the coefficients as the following:

$$c_1 = T_0 + \frac{\alpha P K_0(\gamma_R)}{2\pi R t K_1(\gamma_R)}\sqrt{\frac{t}{G\kappa'}}\left[1 - e^{-\frac{R^2}{r_0^2}}\right] + \frac{\alpha P}{4\pi t\kappa}\left[2\ln(R) - \mathrm{Ei}\left(-\frac{R^2}{r_0^2}\right)\right] \tag{3.12}$$

$$c_2 = -\frac{a r_0^2}{2\kappa} \tag{3.13}$$

$$c_3 = 0 \tag{3.14}$$

$$c_4 = \frac{a r_0^2}{2 R K_1(\gamma_R)}\sqrt{\frac{t}{G\kappa'}}\left[1 - e^{-\frac{R^2}{r_0^2}}\right] \tag{3.15}$$

Under these constant, using Eqs. 3.6 and 3.7 we can find the radial thermal distribution. Figure 3.1 shows the temperature distribution map for a typical material illuminated under 70 μW.

3.2.3 *Calculating the Thermal Conductivity via the Bolometric Effect*

The key element in the bolometric thermal conductivity measurement method is the calculation of the temperature dependent resistance change over the sample. As mentioned earlier, every material shows temperature dependent electrical resistance change to a certain extent. For metals, in the vicinity of the room temperature, the change is linear in temperature and very predictable. A resistivity-temperature measurement around the room temperature gives how overall resistivity of the material changes. This change can be correlated with the change over the suspended part of the material for the bolometric effect based thermal conductivity measurement method. Here, the aim is to fit the thermal conductivity value to the set of equations we will derive in the following part to measured resistivity change over the center of the hole (Fig. 3.2).

The challenge is calculating the total resistance change of the device when the laser is at the center of the suspended part of the crystal. If we assume that the center of the hole is at $\mathbf{r} = 0$, then the resistivity distribution can be written as $\rho(\mathbf{r}; T(\mathbf{r}))$. For a resistivity distribution over a 2D material the electrical current flow has to be solved in between the contacts. For samples with small temperature dependent coefficient of resistance (TCR), the equipotential lines can be assumed to be parallel to the contacts. Thus, by calculating the total resistance of the device by series and parallel addition of infinitesimally small resistive regions and stripes formed by these regions gives the total change of resistance. Although it is straightforward, it requires a numerical solution. However, for large TCR samples or measurements with large temperature gradients (i.e. high laser power) the equipotential lines become warped around the suspended part. Thus, the solution offered above is not applicable anymore and the local electric field, $\mathbf{E}(\mathbf{r})$, has to be solved along with the continuity equation for

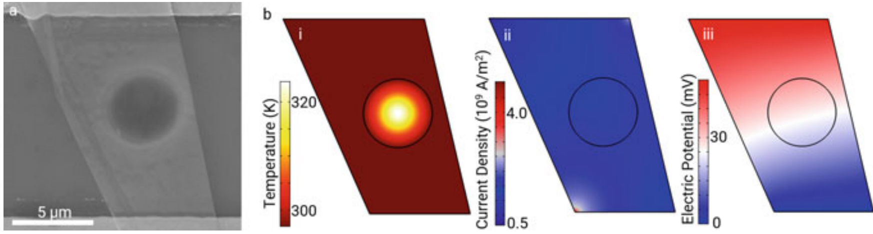

Fig. 3.2 **a** SEM micrograph of a measured 2H-TaS_2 crystal. **b** Thermal simulation of the same crystal, (**b**). Current density under 50 mV bias and **c**. The electric potential distribution over the sample. Notice the slight curvature of the equipotential points over the suspended section of the crystal. Due to increased local resistivity, potential drop is faster. Figure is reproduced from Cakiroglu et al. [1]. Copyright (2020) IOP Publishing

the current density, $\mathbf{J}(\mathbf{r})$. A numerical solution can be obtained for the resistance of the device. However, commercially available finite element method (FEM) solution packages provide a much more convenient way to solve the above problem. In the next section, I will talk about implementation of the problem to the commercially available FEM packages, in particular COMSOL®.

3.3 COMSOL Simulations for Thermal Conductivity Calculation

COMSOL Multiphysics uses finite element analysis to solve coupled differential equations in a wide range of physical problems. For our purposes, we use the Multiphysics and the heat transfer module. We also define the Gaussian laser spot and the heat flux from the laser using equation based solver. The workflow is as the following:

1. Measure the device dimensions. This requires measurement of the sample thickness in a suitable equipment, most typically using atomic force microscopy (AFM). Optical images can be used to measure the lateral size of the crystal.
2. Draw the device geometry in COMSOL with the suspended part defined as a material with different thermal conductivity.
3. Define the heat transfer parameters:
    - Define thermal boundaries
    - Define thermal regions
    - Define the heat in-flux over the suspended circular section.
4. Define the electrical terminals and the electrically isolated edges.
5. Enter the experimentally determined parameters and run the simulation to match the experimentally determined resistance change when the laser spot is at the center of the hole.

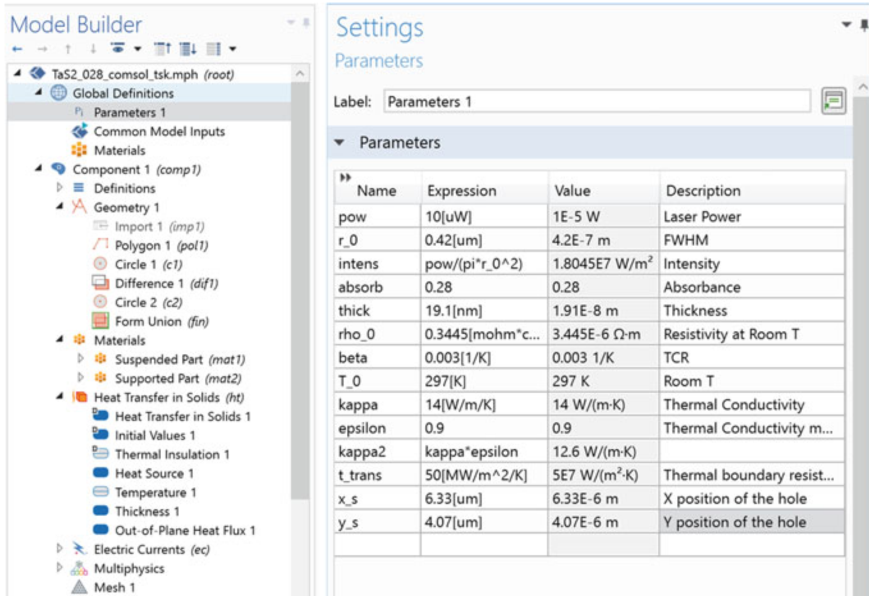

Fig. 3.3 Screenshots from the COMSOL Multiphysics software. Left panel shows the model parameters that are used to create the desired geometry and material parameters for the simulation. There is a single component in the simulation and all the geometries and relevant thermal and electrical boundary conditions are defined over the material. Right panel shows the parameters that are used as the inputs in for the simulation. Here, all the parameters are measured experimentally except the thermal conductivity and thermal conductivity over the supported section of the material. A parametric sweep can be defined in COMSOL to match the experimental δR value

Figure 3.3 shows the model builder and the parameter settings screenshots of the COMSOL graphical user interface. Figure 3.4 shows the model generated for the simulations as well as the multiphysics coupling between the electrical and the thermal simulations for the resistance calculations.

3.3.1 Uniqueness of the Thermal Conductivity Values

One question that begs for an answer is the uniqueness of the obtained thermal conductivity values. We calculated that for a set of κ values, the thermal equation solutions yield a unique δR value. Having a unique value for the resistance change caused by the laser heating is very important for the reliability of the measurement method. Figure 3.5a shows the results of the COMSOL simulations for a set of thermal conductivity values. Another important parameter as discussed in the Sect. 3.4.4 is the absorbance. Figure 3.5b shows the effect of absorbance on the simulated δR value and the fitted thermal conductivity. Moreover, we plotted the thermal profile over the cross-section of the suspended region to show each thermal distribution results in a unique resistivity distribution.

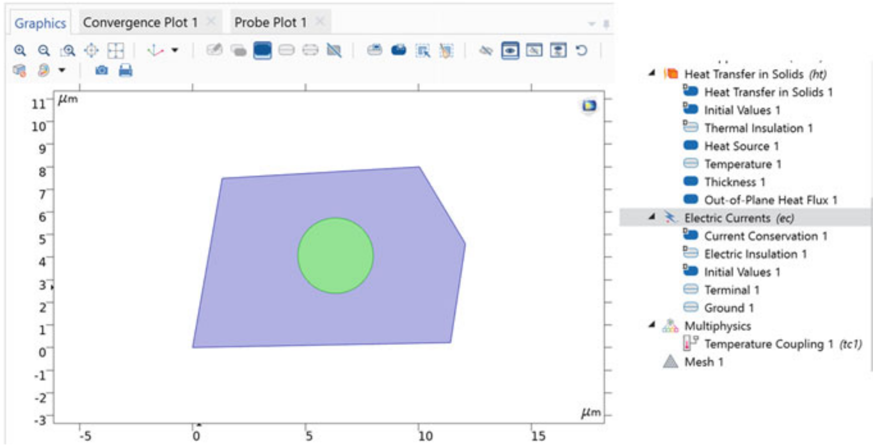

Fig. 3.4 Left panel shows the geometry of the sample defined in COMSOL. Green part at the center is the suspended region of the crystal whilst other regions are supported by a substrate. There is heat loss defined to the substrate in these regions. The panel on the right shows the electrical simulation parameters as well as the temperature coupling multiphysics package that relates the local temperature to the local resistivity of the material and solves for the total resistance of the material under illumination

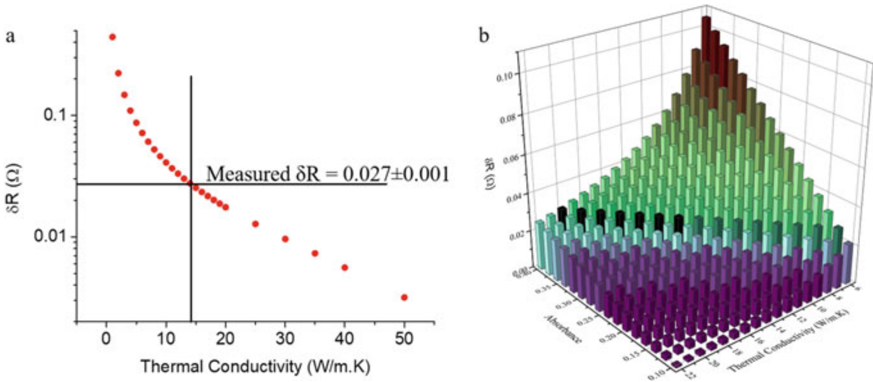

Fig. 3.5 **a** Graph shows how the calculated δR value varies for various thermal conductivity values. It is clear from the solution that there is a unique solution for each κ value. **b** When we vary two parameter at the same time, then we can estimate the propagation of error in the measured quantity to thermal conductivity fitting. Here absorbance is varied. Only the black bars are within the error margin of the measured δR value. Measurement error of the absorbance is less than ±0.03 and this introduces a ±1.0 W/m K error in the thermal conductivity value within the uncertainty of the δR measurements

3.4 Experimental Realization of the Thermal Conductivity Measurements via Bolometric Effect

In this Sect. 3.1 will talk about the experimental methods we use to perform the thermal conductivity measurements via the bolometric effect on 2D materials. These experimental methods include the sample preparation steps for the measurements as well as the experimental setup required for the high sensitivity measurements. First, the fabrication steps for the substrates that are required for the bolometric measurements is going to be discussed. Then, the commonly used transfer methods is going to be introduced. Finally, I am going to introduce the details of the experimental setup for the measurements.

3.4.1 Substrate Preparation

Although it may seem trivial, substrate preparation is a critical step of the bolometric thermal conductivity measurement method. The holes of radius ranging from 0.5 to 1.5 μm has to be drilled over the substrate with high aspect ratio walls. Furthermore, for the electrical resistance change measurements electrical contacts are required. Here, I will discuss various methods to fabricate the substrates for the measurements. The methods vary only with respect to the method the hole is etched on the substrate:

Method 1—With Focused Ion Beam Milling

- Chromium evaporation
- Photoresist spin coating
- Optical pattern forming
- Chromium etch
- Inductively coupled plasma etching by the depth of the metal to be deposited—This step is optional for easier transfer of the crystals on the metal contacts
- Metal deposition and lift-off
- Chromium etch
- Focused Ion Beam drilling of the hole in between the contacts
- Crystal transfer over the contacts and the hole.

Method 2—Without Focused ion Beam Milling

- Chromium evaporation
- Photoresist spin coating
- Optical pattern forming
- Chromium etch
- Inductively coupled plasma etching by the depth of the metal to be deposited—This step is optional for easier transfer of the crystals on the metal contacts
- Metal deposition and lift-off
- Photoresist spin coating

- Optical pattern forming for the holes—aligned with the substrate
- Chromium etch
- Etching of the holes—buffered oxide etch or inductively coupled plasma etch
- Resist removal and chromium etch
- Crystal transfer over the contacts and the hole.

The requirement for the electrical contact deposition introduces new steps as compared to the substrate preparation for the Raman thermometry based measurement technique. However, this is not a major challenge in device fabrication as the steps introduced for the electrical contact formation is a routine for many laboratories working on relevant materials.

The methods discussed above will have different parameters optimized for different systems. Here, the recipes I share are optimized for the equipment located at Bilkent University National Nanotechnology Research Center.

3.4.1.1 Chromium Evaporation

Chromium evaporation is required for forming an hard mask for the etching steps as most of the optical resists get badly damaged during the ICP etching. Si wafer with 1000 nm SiO_2 is cleaned thoroughly using acetone, IPA and water. Then, we evaporate 20 nm thick chromium using electron beam evaporator at a rate of 5 Å per min.

3.4.1.2 Optical Lithography

Once the Cr is deposited on the chips, AZ5209 photoresist is spin coated on and prebaked before UV patterning. AZ5209 is a negative tone resist. The use of negative tone resist is crucial as in the liftoff process they prevent sidewall formation due to undercutting as compared to the positive tone resists. I will refrain from providing a recipe for the optical lithograph process as it is a very generic process. The thickness of the resist is important as the following step requires ICP etching and it is important to have sufficient amount of photoresist left after the etching process. Following the development of the exposed parts, Cr etching is used to expose the surface of the SiO_2.

3.4.1.3 ICP Etching

Inductively coupled plasma etching steps uses CH_3F and O_2. The coil and the plate are operated at 13.56 MHz and 396 KHz at 250 W and 30 W respectively. The process worked at room temperature for 12 min. This etches a pit of depth of 65 nm on SiO_2 surface. This process is important for the metal deposition step to be followed next

as explained in detail. I would like to note that BOE etching would also work for a certain extent as the undercut of the etching will be less than 1% of the width of the unetched gap.

3.4.1.4 Metal Deposition

Following the ICP etching we fill the open holes with Au/Cr. First, 20 nm of Cr is evaporated as an adhesion and filling layer, then 45 nm of Au is evaporated using thermal evaporator. Here, tooling factors of the thickness monitors have to be very accurately determined. Otherwise, there is a great chance of having an under filled or an overfilled hole. Within ±10 nm, metal deposition provides a surface sufficiently flat enough for the crystal transfer. When the depth is not accurately matched, the PDMS stamping transfer fails due to the poor contact of crystal with the substrate. Moreover, it becomes more likely to trap air between the hole and the crystal as well as the edges of the metal contacts and the crystal. Thus, having the correct amount of metal is important for high yield device fabrication and high accuracy thermal conductivity measurements.

3.4.1.5 Focused Ion Beam Milling

A hole between the electrical contacts are required for creating a suspended section of the crystal. For this reason, we used focused ion beam milling. FIB provides a fast and very high aspect ratio way to drill the hole of the desired size. Some examples of the FIB drilled holes in between the metal contact are shown in Fig. 3.6. The major shortcoming of the method is the relative slow speed of the number of holes that can be drilled on a multi-sample chip and FIB is a costly equipment to access and operate.

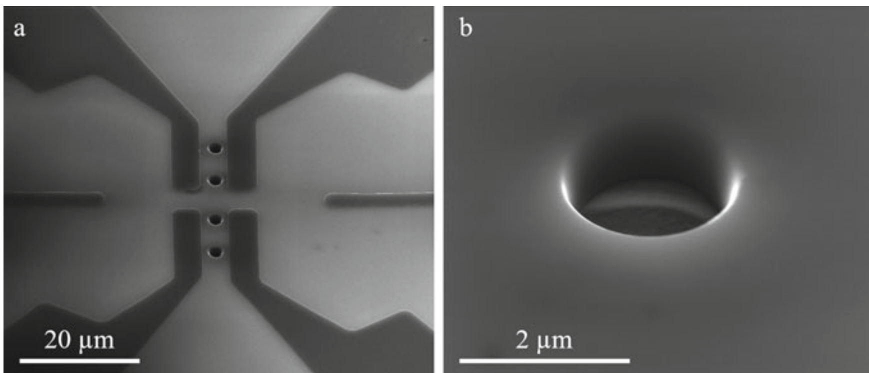

Fig. 3.6 **a** FIB drilled holes between the metal contacts and **b** Close up view of the hole is shown

3.4.1.6 Crystal Transfer

Crystal transfer is an important step. Placing the crystal on the gold contacts with minimal contact resistance is crucial. This has been demonstrated in an earlier study by our group [2]. When the contact resistance dominates the overall resistance of the device, the photoresponse becomes very localised at the contacts and the bolometric response diminishes. Another major challenge is that transferring the crystal over the hole without damaging the suspended section of the crystal. This mandates stamping of the crystal rather than polymer transfer method. A polydimethyl siloxane (PDMS) stamp is prepared using 1:7 ratio mix of the curing agent and the elastomer base. Once the mixture is thoroughly mixed, air bubbles trapped in the mixture are evacuated using a vacuum desiccator. Then the mixture is poured over a glass petri dish cleaned with oxygen plasma. This step is very important for the sake of consistency of the PDMS stamp. Using a PET petri-dish or skipping the plasma treatment results in variation in the stamp properties from batch to batch. This variation determines the overall efficiency of the transfer. With a properly prepared PDMS stamp the yield can as high as 90%, i.e. 9 crystals get successfully adhered to the substrate out of 10 trials. Some research groups use Gel-Pak brand in order to have a reproducible elastic stamp [3]. Mechanical exfoliation of the crystal from the bulk is performed using Nitto brand SPV224 blue tape from the bulk crystals commercially available from hqgraphene.com or 2dmaterials.com. Once, the crystals thinned down to the desired thickness, exfoliation is performed on to the PDMS surface. Thin crystals are identified under an optical microscope. Then the stamp is transferred over a glass slide and the glass slide is attached to a stepper motor driven 3-axis micromanipulator. The target substrate prepared as described in the previous parts is placed on to a heated stage. The crystal is aligned so that the contacts and the hole is centered. Then, by slowly bringing the substrate and the stamp in contact the transfer is performed. Slight heating up to 50 °C is needed for certain crystals to increase the adhesion to the substrate.

To summarize, I would like to emphasize the following points one more time:

- Thin metal contacts, preferably embedded contacts will improve the adhesion of the crystals.
- Stamping of exfoliated crystals provide a break free way of placing the them over the hole
- The whole process can be performed under 10 min from exfoliation to measurement. This minimizes the contact resistance formation as well as protects the device surface from oxidation.

3.4.2 Scanning Photocurrent Microscopy

Scanning photocurrent microscopy (SPCM) is a useful tool to provide the spatial distribution of the photoresponse of a material. A focused laser spot, raster scanned

over a sample with metal contacts allows the creation of a photocurrent map. The setup is typically composed of a laser beam modulated at a specific frequency f. This frequency is fed to a lock-in amplifier and the output of a current preamplifier is attached to the input of the lock-in amplifier to measure the signal induced by the laser beam. This ensures that only the laser-induced photocurrent is measured. For feasible enough scanning speeds, typical integration time of 3 ms is chosen. Thus, any photoresponse mechanism that leads to photocurrent generation faster than 3 ms can be measured. Various wavelengths can be employed in SPCM measurements. Of course, depending on the wavelength of the laser used, the minimum feature size that can be resolved varies.

Laser scanning in a typical SPCM setup, the laser beam is focused on to the sample using a high resolving power objective. Typically we use a 40× objective. This creates a spot size of 400 nm FWHM for a 532 nm laser wavelength. The scan can be performed in three different ways. First, a galvo-mirror pair can be used to steer the light over the entrance pupil of the objective and this can move the focused spot on the sample. The range of the motion is limited to the size of the entrance pupil. Second scanning method can be scanning the objective. This is similar to the galvo-scanning, however in this method, the objective is attached to a scanner and the steering of the laser beam is performed by the motion of the objective with respect to the fixed laser beam. The third method would be scanning the sample with all the optics held fixed. This method increases the stability of the optical path at a cost of reduced reduced scan range. The setup we use is a commercially available setup from a start-up company where they compacted all the optics so that the whole scanning is performed by a moving microscope. This allows a very large range of motion, which becomes very handy when there are multiple samples on a chip inside the cryostat. The schematic and the picture of the setup is shown in Fig. 3.7.

Lock-in amplification for a sensitive measurement of the resistance change, we use the lock-in amplification scheme. Lock-in amplifier uses the orthogonality of a single frequency component to other harmonics in a noisy signal to extract the signal to be measured even the noise is about 1000 times larger than signal to be measured. Since lock-in method is an ac measurement technique, any slow varying or dc component of the signal is also rejected. Thus it is possible to measure the effects only induced by the laser.

The photocurrent is measured from two terminals on the sample. The voltage bias can be applied from one of the contacts and the other contact acts as a virtual ground, connected to a current pre-amplifier. We use SR-560 as the current pre-amplifier. Although it is not mandatory it serves two purposes. First, it is a very low impedance equipment and can operate in a very large range device resistances, from a few ohms to hundreds of megaohms. Second, there are configurable filters that helps rejection of the signal that is out of the frequency band of interest. Another way to use SR-560 is to use it as a voltage bias source and have a real ground on the other terminal. It provides a voltage output resolution of 0.5 mV, which is adequate for many measurement scenarios. SR-560 outputs the amplified signal from −5.4 to 5.4 V depending on the sign of the measured current. This signal is fed to the

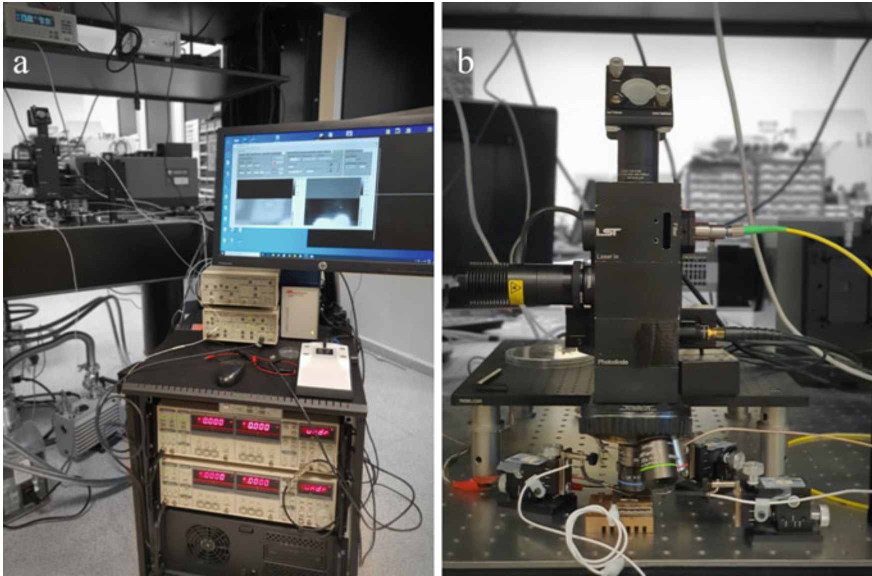

Fig. 3.7 **a** Photograph of the control box for the SPCM setup. **b** Close-up shot of the SPCM scanning head. The copper stage at the base is a Peltier stage with heating and cooling. Electrical probes are used for the photocurrent measurements

lock-in amplifier's voltage input. The laser beam is typically chopped around a kHz. This is slow enough for many processes, but sufficiently fast to reject any common noise sources like the line noise or its higher harmonics. The chopping can be both done electronically, with TTL output from the lock-in amplifier or with a mechanical chopper in the optical path, whose frequency is fed to the lock-in amplifier as the reference signal. Thus, the lock-in amplifies the signal that is resulting from the referenced laser beam. This, combined with the scanning motion allows the creation of the spatial photocurrent map. Here, the scanning has to be performed slower than the integration time of the lock-in. Typically we scan with a rate of 10 ms per pixel. Thus, we limit the integration time to maximum of 3–10 ms. Anything faster than 3 ms results in large noise for small currents.

Creating an intensity map from the reflected light to be able to correlate the photocurrent map to the parts of the sample, an intensity map from the reflected light is mandatory. This is done by placing a photodiode in the reflected light path. Since the laser beam is chopped, it is necessary to measure the signal with a lock-in amplifier as well. If cost of the setup is a concern, a phase locked loop that can be purchased in the form of audio amplifier serves the same purpose as the signal output of the photodiode is already significant enough. Another method would be tuning the frequency of the chopping and the scan rate so that there is enough intensity in every pixel. However, this would require a very stable mechanical chopper or a

TTL source. The reflection map also serves to determine the beam size using the knife-edge method. Spatial derivative of the intensity line trace from the edge of a beyond resolution limit metal contact provides a method to determine the FWHM of the laser spot.

Collection of the data we use LabView from National Instruments for the collection of the data since the ecosystem contains all the require drivers for instrument communication and the learning barrier for the programming with graphical user interface is very low. Furthermore, modifications to the software is very straightforward and can be done on the fly. However, Matlab or any other coding language can be used for the collection of the data. The software should do the following tasks:

- Control the scan in x-y direction with control over the scan size and the step size
- Control the experimental parameters such as the applied bias, instrument sensitivities etc.
- Collect and display the data in real time. This is very important as each fine scan takes around several minutes.
- Record and -preferably- analyse the data.

The intensity map and the corresponding photocurrent map provides a diffraction limited resolution information about the light induced electrical current. Thus the origin of the photoresponse can be identified by analysing the data.

3.4.3 Determining the Full Width-Half Maximum Value for the Focused Laser Spot

There are various tools for determining the profile of a laser beam as simple as a CMOS camera. However, I would like to introduce a method that is commonly used to determine the full width at half maximum (FWHM) of a Gaussian laser beam. As our method significantly benefits from scanning of the sample due to increased number of data points from the center of the suspended region, corresponding reflection map is produced for spatial confirmation of the position of the hole. Gold contacts with a large aspect ratio, allows a knife-edge determination of the laser profile. The position derivative of the line trace taken along the edge of the gold contact in the intensity map gives the cross-section of the laser beam. Gaussian fitting to the $\frac{\partial I}{\partial x}$ versus x plot yields the FWHM value for the laser spot. This might seem like a trivial aspect of the experimental scheme we proposed, however, on the contrary it significantly affects the uncertainty in the determination of the thermal conductivity value as r_0 is an input parameter in both Eqs. 3.3 and 3.4. Figure 3.8 shows the knife-edge determination of the laser FWHM.

In our experimental setup we use a 40x ultra-long working distance objective with slip-cover compensation up to 2 mm from Olympus. This objective pointed through a 1 mm sapphire window yields 430 nm FWHM for 532 nm laser. This is quite acceptable for an objective with 0.6 NA. Further improvement is possible if a higher magnification objective with larger numerical aperture is used.

Fig. 3.8 **a** SEM micrograph of a 2H-TaS_2 crystal over the contacts. **b** SPCM reflection intensity map of the same crystal. Red dashed line shows the line trace given in **c** First derivative of the reflection intensity with respect to the position gives two Gaussian peaks. Gaussian fits to the peaks give the full width at half maximum value for the laser spot

3.4.4 Determining the Absorbance of the Material

Perhaps one of the most challenging aspects of the bolometric method is the measurement of the absorbance, α, of the material under investigation. For many materials, in particular for 2D materials, α is unknown. Moreover, it strongly depends on the number of layers when crystals are thinned to the monolayer limit. To measure the absorbance, we use the following method: First exfoliate the crystal on a transparent substrate. PDMS is a better choice as the thin flake identified on the PDMS stamp can later be transferred over the device for the thermal conductivity measurements. The laser intensity, I_0 is measured using a powermeter or a CCD camera attached to a spectrometer. Then, the transmitted intensity, T_0, is measured over the PDMS surface next to the specified crystal followed by the measurement of the transmitted intensity over the crystal, T. Finally, the reflected intensities from the bare PDMS surface, R_0, and the crystal surface, R, are measured. A schematic of the setup is shown in Fig. 3.9. Absorbance can be calculated from the quantities as the following:

$$\alpha = \frac{I_0 - (T + R) - (T_0 + R_0)}{I_0} \tag{3.16}$$

This measurement ensures that the correct ratio of the laser power absorbed can be used in the fitting of the experimental data. Even though for many materials α is temperature independent for a large range of temperatures, one has to be careful in particular when working with materials that show phase transitions which can significantly alter the absorbed laser power.

In our recent study, to measure the absorbance of 2H-TaS_2 for the first time we used a setup similar to that is described in the previous paragraph. The optical connection to the spectrometer is made through a multimode optical fiber with 200 μm core diameter. The end of the fiber is placed in contact with the 0.5 mm PDMS piece. The crystal is centered with the center of the fiber core to ensure maximum amount of light coupling to the fiber. The other end of the fiber is connected to an Andor

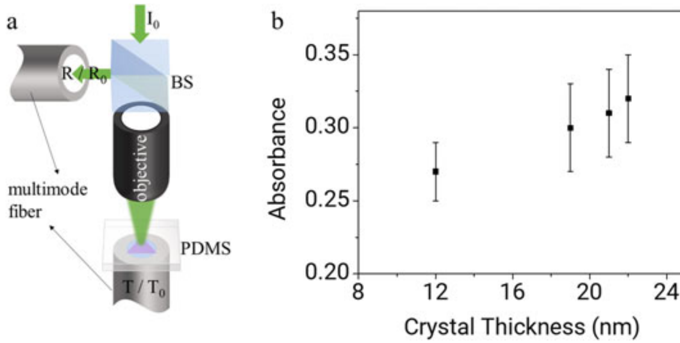

Fig. 3.9 **a** Schematic of the absorbance measurements is given in the figure. Both the transmitted light and the reflected light are measured using a spectrometer. **b** Thickness dependent absorbance of 2H-TaS_2 crystals. Data from

Shamrock 500i spectrometer equipped with iDus 400 CCD camera. We used 150 lines/mm diffraction grating to collect the intensity. As the optical losses within the spectrometer is the same for all measurements this is not too critical, however having the best possible signal to noise ratio decreases the measurement errors.

The effect of α on the thermal conductivity measurements is limited. COMSOL simulation in Fig. 3.5 shows how error in α propagates to the measured thermal conductivity value.

3.5 Extending the Bolometry Based Thermal Conductivity Measurements to 3D

It is possible to extend the methodology of the bolometry based thermal conductivity measurement method to take measurement in three-dimensional samples. The assumption we make in 2D bolometric measurements is that laser power is absorbed more or less uniformly through the thickness of the material and the absorbed heat from this point spreads uniformly through the sample in-plane axis. When the sample becomes thick enough, it is possible to model the thermal distribution in 3D. For thermally isotropic materials modelling the temperature distribution, thus the resistivity distribution is straightforward with the known optical absorbance of the material. Thermal conductivity can be measured using the method. For the bulk of 2D materials, anisotropy of the thermal conductivity is very large and this would require simultaneous fitting of both in-plane and cross-plane thermal conductivity values to match the experimentally measured resistance change. Thus, the uniqueness of the resistance solution will be questionable as there will be a set of thermal conductivity values that may give the same resistance change under the illumination. One solution to this problem could be measuring the in-plane thermal conductivity

of a thin enough for uniform depth heating (but thick enough to be considered as bulk), then using the this value to find the cross-plane thermal conductivity in thicker samples. More experiments have to be conducted to fully understand the limitations of the bolometric method extended to 3D.

3.6 Extending the Bolometry Based Thermal Conductivity Measurements to 1D

The solutions of the heat equation becomes much simpler in 1-dimensional heat transport. In an earlier work [4], we used the thermal conductivity of VO_2 nanowires to calculate the bolometric resistance change. At the time the photoresponse mechanism for VO_2 was unknown, however, revealing the bolometric nature of the photoresponse shows us that whenever the photoresponse mechanism is known, it is possible to use the that to extract the thermal conductivity. 1D heat transport solutions can also be used in 2D materials with in-plane thermal conductivity anisotropy such as black phosphorus [5] when combined with clever measurement strategies. Rather than a Gaussian laser spot, a line shaped illumination along the crystal width can be used to extract the thermal conductivity along a certain axis of the crystal.

1D heat equation ignoring the Newtonian cooling and heat loss by radiation can be written as:

$$\kappa \frac{d^2 T_1(x)}{dx^2} + \frac{I\alpha}{t} e^{-x^2/w_0^2} = 0 \qquad x < w \tag{3.17}$$

$$\kappa' \frac{d^2 T_2(x)}{dx^2} - \frac{G}{t}(T_2(x) - T_0) = 0 \qquad x > w \tag{3.18}$$

Here, w is the width of the suspended part of the crystal. All other parameters are defined in Sect. 3.2.2. General solutions to the above equations are:

$$T_1(x) = C_1 + C_2 x - \frac{a\sqrt{\pi} w_0}{2\kappa} \left(\frac{w_0}{\sqrt{\pi}} e^{-x^2/w_0^2} + erf(\frac{x}{w_0}) x \right) \tag{3.19}$$

$$T_2(x) = T_0 + C_3 e^{x\sqrt{\frac{G}{t\kappa'}}} + C_4 e^{-x\sqrt{\frac{G}{t\kappa'}}} \tag{3.20}$$

where erf is the error function and C_i are constants of integration. When we introduce the following boundary conditions, we can write the solutions of the differential equation:

$$(i) \qquad T_2(x \to \infty) = T_0 \tag{3.21}$$

$$(ii) \qquad \left. \frac{dT_1(x)}{dx} \right|_{x \to 0} = 0 \tag{3.22}$$

$$(iii) \qquad \kappa \frac{dT_1(x)}{dx}\bigg|_{x\to w} = \kappa' \frac{dT_2(x)}{dx}\bigg|_{x\to w} \tag{3.23}$$

$$(iv) \qquad T_1(x)|_{x\to w} = T_2(x)|_{x\to w} \tag{3.24}$$

First and the second boundary conditions suggest that when we are sufficiently far away from the laser beam, temperature of the crystal equilibriates with the ambient and the temperature under the laser spot is finite. Third and the fourth boundary conditions imply that the temperature at the interface of the supported and the suspended parts are at the same value with incoming and outgoing energies are the same. It is also possible to solve Eq. 3.17 without including the Gaussian heating term and adding the laser power in (3.22). Also, it is possible to include a Newtonian cooling term for measurement under the ambient, which becomes relevant especially when the sample is suspended over a substrate. Under the boundary conditions we obtain the following integration constants:

$$C_2 = C_3 = 0 \tag{3.25}$$

$$C_4 = \frac{\alpha w_0}{2}\sqrt{\frac{t\pi}{G\kappa'}}\frac{erf\left(\frac{w}{w_0}\right)}{e^{-wG/t\kappa'}} \tag{3.26}$$

$$C_1 = T_0 + C_4 e^{-w\sqrt{G/t\kappa'}} + \frac{\alpha\sqrt{\pi}w_0}{2\kappa}\left(\frac{w_0}{\sqrt{\pi}}e^{-\frac{w^2}{w_0^2}} + erf(w/w_0)w\right) \tag{3.27}$$

Similar to the 2D case, using the thermal solution it is possible to find the resistivity distribution $\rho(x)$. In this case, there is no need to use FEM simulation as the total resistance of the device can be found easily by integrating the resisitvity along the length of the 1D crystal.

Here, I would like to study a hypothetical 1D metallic crystal that is 10 µm long, 0.5 µm wide and 20 nm thick. I assume that the length of the crystal is suspended across the metal contacts, thus the ends are both thermally and electrically in equilibrium with the metal contacts. I assumed heat convection to the ambient and I performed a parametric sweep on the thermal conductivity values to get the temperature distribution on the sample and the resistance change of the crystal. Figure 3.10 shows the plots for each thermal conductivity value running from 1 to 50 W/m K.

3.7 Measuring Thermal Conductivity of Semiconductors

Although intrinsic semiconductors show bolometric response that is well defined with the Arrhenius relation, due to lack of a local heating mechanism other than optical, the use of the bolometry based thermal conductivity measurement method is not straightforward. In this section, I would like to discuss the applicability of the method on 2D semiconductors.

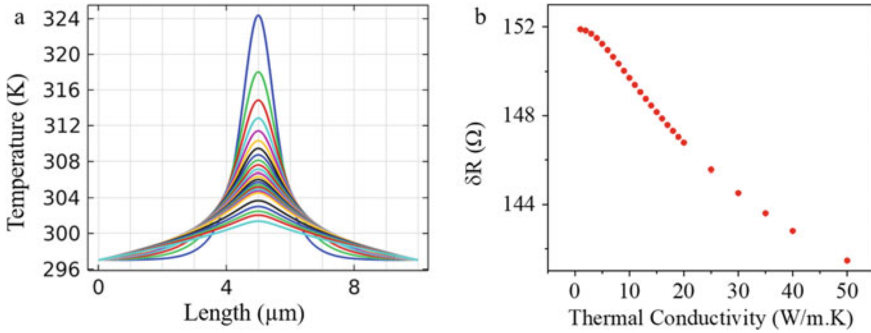

Fig. 3.10 **a** Temperature distribution along the width of the crystal for various thermal conductivity values ranging from 1 to 50 W/m K. As the thermal conductivity increases, the peak temperature decreases but the overall temperature of the crystal rises. **b** Change in the resistance shows unique values for each thermal conductivity value ensuring that the measurement will return a single value

There are various mechanisms for photo-generated currents in semiconductors. For the timescales shorter than a millisecond that is relevant to the timescale of our measurement method, photoconductivity in a semiconductor under bias can result from the formation of non-equilibrium carriers due to light absorption, separation of non-equilibrium carriers due to built-in electric fields or photothermal effects. Each of these effects has to be distinguished from each other to use the bolometric response as a local temperature probe. Moreover, when a 2D material is suspended there might be strain induced built in electric fields that may result in complicated non-equilibrium carrier separation patterns. Figure 3.11 shows the data collected on a multilayer (12 nm thick) WS_2 crystal. In particular variation in the photoconductance at different biases indicates coexistence of various photoconductance mechanisms. Still the calculations for the thermal conductivity gives 8 W/m K which is slightly lower that what has been reported in the literature [6].

We also performed SPCM on MoS_2 crystals. However, we obtained a very interesting zero bias photoresponse over the suspended part of the crystal as shown in Fig. 3.12c. We hypothesize that the unique photoresponse emerges due to the stress induced electric field with in the suspended part of the crystal that results in separation of the non-equilibrium carriers induced by the optical excitation. When the bias is applied, photoresponse is as complicated as the 0 mV bias and extracting the sole bolometric effect is not possible. These initial measurement on the semiconducting materials clearly show the need for very careful measurements to extract the bolometric effect out of other photoconductance mechanisms. However, this may not be a straightforward task and one might be better off with other measurement methods on semiconductors. I would like to emphasize one distinction here regarding the nature of the energy gap. For materials that can be described by single-electron models within the Fermi-liquid theory, considerations I made above are valid. However, for materials such as VO_2 where the insulating gap opens due to strong electronic cor-

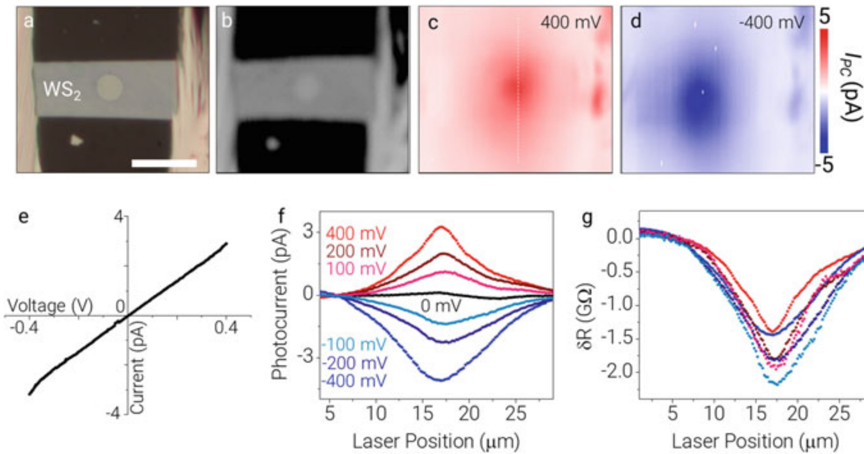

Fig. 3.11 **a** Optical microscope image of a multilayer WS_2 crystal contacted with indium needles. Scale bar is 10 μm. **b** Reflection map and **c**, **d** corresponding photocurrent maps taken at 400 mV and −400 mV respectively. **e** IV plot is mostly linear indicating small barriers at the indium contacts. **d** Line trace taken along the width of the crystal shows the photoresponse through the suspended part of the crystal under different biases. **f** Photoconductance shows slight variation under different biases hinting existence of another mechanism that might be producing current beyond the bolometric effect. Reprinted with permission from Cakiroglu et al. [1]. Copyright (2020) IOP Publishing

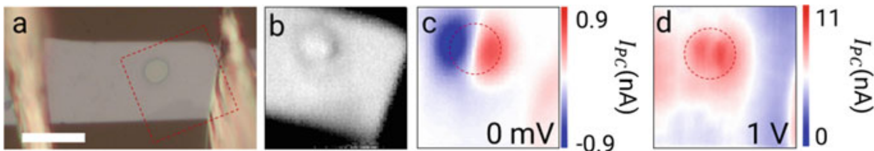

Fig. 3.12 **a** Optical microscope micrograph of a 10 nm thick MoS_2 crystal contacted with indium needles. **b** SPCM reflection map and **c**, **d** corresponding photocurrent maps at 0 and 1 V biases. Notice bipolar photoseponse from the suspended part of the crystal. Reprinted with permission from Cakiroglu et al. [1]. Copyright (2020) IOP Publishing

relations since the thermalization happens very rapidly within less than the length of a unit cell, bolometry based thermal conductivity measurement method will still be applicable in these materials.

3.8 Concluding Remarks

In this brief I tried to introduce the recent literature on the thermal conductivity of 2D materials including our recent contribution. 2D materials field is still an emerging field and for the reasons mentioned in the first chapter, the number of studies in the

field is growing exponentially with many papers appearing every day. It is nearly impossible to capture all the literature in a brief of this nature. Thus, I had to narrow down the topic to the single crystalline 2D materials and skipped the literature entirely on multi-crystalline 2D materials and composites of 2D materials. Furthermore, I omitted the discussions that might be relevant to the thermoelectric energy harvesting. Bi_2Te_3 as an instance layered material that shows exceptional figure of merit for the thermoelectric energy harvesting, however I omitted any discussion on such materials out of the scope of this brief. I tried to provide as many details as possible that is relevant to the theoretical discussion of the thermal conductivity in 2D materials and the experimental methods. Moreover, I believe the method we introduced is superior to other available methods in the literature in certain aspects. Thus I tried to provide an in depth introduction of the method with all the details that can not be provided in a short journal paper here. I hope this will help other researchers to understand, apply and improve the bolometry based thermal conductivity measurement method. To conclude, there are still a lot that can be learned on the thermal properties of the 2D materials. For instance, there is no comprehensive study on the thermal properties of the Moire superlattices. Any theoretical and experimental work on such systems may open new opportunities in tunable thermoelectric systems.

References

1. Cakiroglu O, Mehmood N, Çiçek MM, Aikebaier A, Rasouli HR, Durgun E, Kasirga ST (2010) 2D Materials (Dec 2016), 11. https://doi.org/10.1088/2053-1583/ab8048. https://iopscience.iop.org/article/10.1088/2053-1583/ab8048
2. Mehmood N, Rasouli HR, Çakıroğlu O, Kasırga TS (2018) Phys Rev B 97(19):195412. https://doi.org/10.1103/PhysRevB.97.195412
3. Castellanos-Gomez A, Buscema M, Molenaar R, Singh V, Janssen L, Van Der Zant HS, Steele GA (2014) 2D Materials 1(1). https://doi.org/10.1088/2053-1583/1/1/011002
4. Kasırga TS, Sun D, Park JH, Coy JM, Fei Z, Xu X, Cobden DH (2012) Nat Nanotechnol 7(11):723. https://doi.org/10.1038/nnano.2012.176. http://www.nature.com/articles/nnano.2012.176
5. Luo Z, Maassen J, Deng Y, Du Y, Garrelts RP, Lundstrom MS, Ye PD, Xu X (2015) Nat Commun 6(1):8572. https://doi.org/10.1038/ncomms9572. http://www.nature.com/articles/ncomms9572
6. Zobeiri H, Wang R, Zhang Q, Zhu G, Wang X (2019) Acta Materialia 175:222. https://doi.org/10.1016/j.actamat.2019.06.011. https://linkinghub.elsevier.com/retrieve/pii/S1359645419303702